Pressurizing the van der Waals magnet FeOCl at low temperatures: Phase transitions and structural evolution

Achim M. Schaller,[1] Maxim Bykov,[2] Elena Bykova,[2] Konstantin Glazyrin,[3] and Sander van Smaalen[1,*]

[1]*Laboratory of Crystallography, University of Bayreuth, 95440 Bayreuth, Germany*

[2]*The Earth and Planets Laboratory, Carnegie Institution for Science, Washington, DC 20015, USA*

[3]*Deutsches Elektronen-Synchrotron DESY, Notkestr. 85, 22607 Hamburg, Germany*

(Received 1 March 2022; accepted 10 May 2022; published 19 May 2022)

Magnetic order is frustrated on the orthorhombic lattice of van der Waals layered FeOCl. Antiferromagnetic (AFM) order is attained at ambient pressure upon cooling through $T_N = 81$ K, due to an accompanying monoclinic lattice distortion lifting the magnetic frustration. Within the paramagnetic state at 293 K, an incommensurate structural modulation appears above a critical pressure of $p_c \approx 15$ GPa, while orthorhombic symmetry is retained. This modulation is related to an optimization of the packing of chlorine atoms within the van der Waals gap. Here, we report four new phases in the pressure-temperature (p, T) phase diagram of FeOCl below room temperature. High-pressure–low-temperature single-crystal x-ray diffraction (SXRD) up to 37.8 GPa reveals that, at 100 K, the AFM transition occurs at $p = 7.3 \pm 1.3$ GPa. The pressure coefficient of $\Delta T_N/\Delta p = 2.13$ K/GPa explains that FeOCl remains paramagnetic up to the highest measured pressure of 33.3 GPa at 293 K. At 6 and 100 K, the structural modulation appears around $p_c \approx 15$ GPa within the AFM ordered phase with monoclinic symmetry. The monoclinic and triclinic lattice distortions increase with pressure up to $\gamma = 90.64(1)^\circ$, much larger than the maximum value of 90.1°, that can be reached upon cooling at ambient pressure. The structural evolution provides the geometrical basis for the increase with the pressure of direct $3d$-$3d$ exchange and superexchange interactions. It is proposed, that a strong monoclinic lattice distortion may be of importance for understanding the properties of single-layer FeOCl materials.

DOI: 10.1103/PhysRevB.105.184109

I. INTRODUCTION

The isostructural compounds MOCl, with M = Ti, V, Cr, Fe, crystallize in the orthorhombic FeOCl structure type. The crystal structures consist of double layers of highly distorted MCl_2O_4 octahedra, which are stacked along the **c** axis (Fig. 1).

Consecutive layers are connected via Cl$\cdots$Cl van der Waals bonds. These transition-metal oxychlorides have been in the focus of research since several decades, including experimental and computational studies on the nuclear and magnetic crystal structures and electronic structures, as well as studies of their physical properties [3–7]. From this work, it became apparent that MOCl compounds are low-dimensional magnetic materials. Their magnetic properties can be rationalized in terms of orbital order of the different numbers of $3d$ electrons of M^{3+}. The $3d^1$ electronic configuration of Ti^{3+} is responsible for strong direct exchange interactions between Ti^{3+} ions along the **b** axis. This makes TiOCl a quasi-one-dimensional magnetic compound [4] that develops a spin-Peierls state at low temperatures [3,4,8] and at low-temperature high-pressure conditions [9]. The situation is different for MOCl-compounds with more than one $3d$ electron, where strong magnetic interchain interactions lead to quasi-two-dimensional (2D) magnetic behavior and different phase diagrams [10–13]. VOCl ($3d^2$), CrOCl ($3d^3$) and FeOCl ($3d^5$) develop antiferromagnetic (AFM) order at low temperatures, which is, in each case, accompanied by a monoclinic lattice distortion that lifts the frustration of magnetic order within the layers of the orthorhombic crystal structure [10–13]. This magnetoelastic coupling is distinctive for MOCl, and the monoclinic distortion can be considered an order parameter [13]. For FeOCl, the transition to the AFM state is observed at a Néel temperature of $T_{N,1\,\mathrm{bar}} = 81$ K at ambient pressure [13].

Aside from the strong interest in the fundamental physics of MOCl compounds, a renewed interest in the application of FeOCl-type compounds resulted in reports about the use as catalysts [14–17], nonlinear optical materials [18], and developments in the context of chloride ion batteries [19–23]. Research on this specific class of compounds was further boosted by the proposal of MOCl as van der Waals heterostructures [24], and their use as two-dimensional (2D) intrinsically magnetic monolayer materials, e.g., for applications in the field of spintronics [25–31]. Zhang *et al.* [32] reported liquid exfoliation of FeOCl into few-layer thick nanosheets, a feature that was explained by the low cleavage energy of 340 mJ m^{-2} being close to the value of 320 mJ m^{-2} for graphite. In two-layer-thick nanosheets of FeOCl, a phase transition at $T_{2L,1\,\mathrm{bar}} = 14$ K to a canted antiferromagnetic state was found to replace the AFM transition in bulk FeOCl at $T_{N,1\,\mathrm{bar}}$ [33]. In contrast to those observations on nanosheets, it has been concluded that the Néel temperature of monolayer FeOCl, which is computed to be $T_{mL,1\,\mathrm{bar}} =$

*smash@uni-bayreuth.de

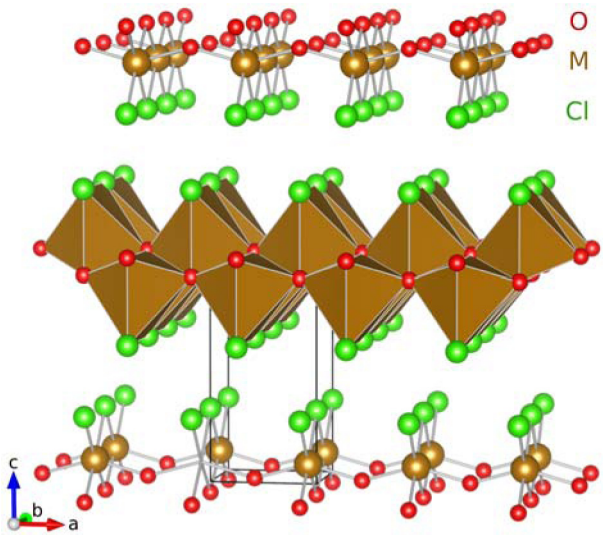

FIG. 1. Perspective view of the crystal structure of FeOCl with space group *Pmmn* at ambient conditions [1]. The unit cell is indicated by solid (black) lines. Distorted MCl_2O_4 octahedra are displayed for the central layer. Drawn with the software VESTA [2].

60 K, is closer to the value of the bulk, because of the weak van der Waals interactions between the main layers of the structure [30]. Within the context of recent progress towards nanosheet materials of FeOCl, the fundamental interplay between pressure-controlled structural changes and magnetic oder in *M*OCl-type compounds may not only contribute to the understanding of the low-dimensional magnetic van der Waals systems in general, but may also have ramifications for the field of 2D based materials and their applications.

The interplay of magnetic order and structural changes can be investigated by the application of pressure. In case of FeOCl, pressure-induced changes in bond lengths and bond angles may modify Fe–Fe exchange and Fe–O–Fe superexchange interactions. This may lead to a strong pressure dependence of the Néel temperature [34–40]. An increase of T_N with increasing pressure is indeed expected from Bloch's empirical rule about the volume dependence of superexchange interactions, as derived from experimental results of transition-metal based insulators [41]. However, pressurizing FeOCl at room temperature does not lead to a magnetically ordered state. Instead, structural phase transitions have been observed at $p_c \approx 15$ GPa towards similar incommensurately modulated crystal structures for all *M*OCl compounds [42,43]. This transition is the result of a densification of the van der Waals interlayers, while maintaining favorable Cl$\cdots$Cl interatomic distances [42,43]. This transition is not the result of magnetic order [42], but it is a purely structural effect, instead. The lattice of FeOCl remains orthorhombic in the structurally modulated phase at high pressures and room temperature. The modulation is characterized by the wave vector $\mathbf{q}_X = (\sigma_1, 0, 1/2)$, where $\sigma_1 = 0.260$ is incommensurate at 15 GPa. The modulation is commensurate with $\sigma_1 = 1/4$ for pressures above 22.7 GPa [42,43].

Here we report the results of pressure-dependent, single-crystal x-ray diffraction on FeOCl at temperatures above and below $T_{N,1\,\mathrm{bar}}$ for pressures up to 37.8 GPa. We show that the transition to the AFM state exhibits a strong pressure dependence, and that the characteristic monoclinic lattice distortion of the AFM state is significantly enhanced at elevated pressures. The structural transition takes place at low temperatures at similar critical pressures as has been found at room temperature. However, at low temperatures, it involves the formation of a modulated structure with monoclinic symmetry instead of orthorhombic symmetry at room temperature. We analyze and discuss the possible effects of the lattice and structural changes on the magnetic interactions in FeOCl. It is suggested that the strongly enhanced monoclinic lattice distortion in the AFM state might be of importance for understanding magnetic behavior of single-layered FeOCl and nanosheet FeOCl.

II. EXPERIMENT

A. Sample preparation

Single crystals of FeOCl were prepared by vapor transport [1] in an evacuated quartz-glass ampoule from a stoichiometric mixture of $FeCl_3$ (99.7% purity, ChemPur) and Fe_2O_3 (99.999% purity, abcr). The ampule was heated and subsequently kept for 65 hours at a temperature of 663 K, followed by slow cooling to 293 K over 5 hours. The reaction resulted in transparent red to brown, plate-like crystals of FeOCl, spread over the length of the ampoule. Single crystals of suitable sizes were selected for the diffraction experiments.

B. Cryogenically cooled diamond anvil cells

Diamond anvil cells (DACs) were employed, which contained Boehler-Almax anvils with culets of 300 μm in experiment 1 and of 400 μm in experiment 2. Sample chambers with approximate diameters of 150 and 200 μm were drilled into preindented rhenium gaskets with initial thicknesses of 35 and 80 μm, respectively. FeOCl single crystals with dimensions of 55×55 μm^2 (1) and 135×80 μm^2 (2) and a thickness of 5–10 μm were loaded into the DACs, together with a ruby sphere for *in situ* pressure determination, and a piece of tungsten for alignment purposes. Neon served as a pressure-transmitting (PTM) medium.

The membrane-driven cells were mounted into a copper block connected to a He cold finger cryostat [44] and cooled with a rate of 3 K min^{-1}. This was followed by a stabilization time of more than one hour at $T = 100$ K (1) and 6 K (2).

Upon increasing the pressure in the second experiment, the temperature increased to approximately 8 K at 14.5 GPa and it was kept at this temperature for the remaining pressure points in this series. We note that the lowest reachable temperature with this system strongly depends on the thermal contact between the different parts of the DAC and the cryostat as well as on the heat exchange with the environment. This may introduce discrepancies between the temperatures at the sample and at the position of the temperature sensor. In order to minimize this difference, the thermal contact was optimized by placing thin Indium foils between the different parts of the setup, while heat exchange with the environment was minimized by applying a vacuum of 10^{-5} bar in the cryostat housing.

TABLE I. Characteristic properties of the eight phases in the (p, T) phase diagram of FeOCl. Given are the number of the phase (No.) (compare to Fig. 2), the lattice symmetry, the space group or superspace group (SSG) [49], the modulation wave vector of the nuclear modulation ($\mathbf{q}_X$) (compare to Fig. 4), and the pressure (p) ranges of each phase at the three temperatures for which experimental data are available.

				observed pressure range (GPa)		
No.	Lattice	SSG	$\mathbf{q}_X$	293 K	100 K	6 K
I	orthorhombic	59 *Pmmn*	—	$0 < p < 14.0$	$0 < p < 6.3(3)$	—
II[a]	monoclinic	13.1.2.1 $P2/n(\alpha, \beta, 0)$	$(0, \sigma_b, 0)$	—	$8.9(7) < p < 13.9(1)$	$0 < p < 12.6(1)$
III[b]	monoclinic	13.1.3.2 $P2/n(\alpha, \beta, 1/2)0s$	$(\sigma_1, \sigma_2, 1/2)$	—	$p = 17.1(2)$	$14.5(2) < p < 17.8(2)$
IV[b]	triclinic	2.1.1.1 $P\bar{1}(\alpha, \beta, \gamma)0$	$(1/4, 0, \sigma_3)$	—	$20.1(2) < p < 29.1(3)$	—
V[c]	triclinic	2.1.1.1 $P\bar{1}(\alpha, \beta, \gamma)0$	$(1/4, 0, 1/2)$	—	$p = 32.1(3)$	—
VI[c,d]	triclinic		$(1/5, 0, 1/2)$	—	$34.7(2) < p < 37.8(1)$	—
VII[b,e]	orthorhombic	59.1.10.6 $Pmmn(\alpha, 0, 1/2)00s$	$(\sigma_1, 0, 1/2)$	$p = 15.0$	—	—
VIII[c,e]	orthorhombic	59.1.10.6 $Pmmn(\alpha, 0, 1/2)00s$	$(1/4, 0, 1/2)$	$22.7 < p < 33.3$	—	—

[a]Magnetic order in phase II is described by the magnetic modulation wave vector $\mathbf{q}_M = (1/2, 0.275, 1/2)$ at 4.2 K [48]. Notice that $\mathbf{q}_X = 2\mathbf{q}_M$, since $\mathbf{q}_X = (0, 0.555, 0)$ below $T \approx 30$ K [13].
[b]Incommensurate modulation.
[c]Commensurate modulation.
[d]Structure refinement was not possible.
[e]Phases VII and VIII have only been observed at room temperature, i.e., where the structural transition appears within the paramagnetic state [42].

C. X-ray diffraction experiment

High-pressure low-temperature (HPLT) single-crystal x-ray diffraction (SXRD) was measured at beamline P02.2 of the synchrotron PETRA III in Hamburg, Germany, employing monochromatic x-ray radiation with a wavelength of $\lambda = 0.2898$ Å and a beam spot of $H \times V = 6.6 \times 1.9\ \mu\text{m}^2$ [44]. *In situ* HPLT SXRD was measured on compression up to 37.8 GPa at 100 K (experiment 1), and up to 17.8 GPa at 6 K (experiment 2).

Diffracted intensity was collected with a Perkin Elmer XRD 1621 detector upon rotation of the cryostat (including the DAC with the sample) around the vertical axis in a range of $-26 \leqslant \omega \leqslant 26^\circ$ (1) and $-30 \leqslant \omega \leqslant 30^\circ$ (2). Two runs were measured for each pressure point. They involved data collection with continuous rotation with acquisition step size of $\Delta\omega = 0.5^\circ$ and exposure times of 1 and 5 s per frame, respectively. For experiment 2, an additional run was measured with exposure time of 1 s and a Pt foil attenuator in the primary beam. The pressure was determined before and after data collection at each pressure point, employing the online ruby fluorescence system [44,45]. The average pressure of both measurements is used and their difference is included in the uncertainty of the pressure. Additional ruby spheres were put on the table of the diamond facing the detector and online ruby system, in order to collect reference R_1 lines at low temperatures.

D. Phase identification through analysis of x-ray diffraction data

The measured SXRD data were processed with the software CRYSALISPRO [46] for indexing, data integration, data reduction, and absorption correction. For each (p, T) point, this resulted in the lattice parameters and a table of integrated intensities of Bragg reflections. This experimental information was used for crystal structure refinements with the software JANA2006 [47].

Together with previous, temperature-dependent and pressure-dependent diffraction experiments [13,42,48], we have identified a total of eight phases within the (p, T) phase diagram of FeOCl. They comprise orthorhombic, monoclinic (**c** unique) and triclinic lattices, and they differ in the absence or presence of a structural modulation that can be commensurate or incommensurate (Table I). The previous as well as the present diffraction experiments have started with the sample in the orthorhombic *Pmmn* phase at room temperature and low pressure. The other phases have been produced through phase transitions. These have resulted in twinned crystals, in case of lowering of the lattice symmetry. In x-ray diffraction, the pseudomerohedral twinning is visible through split reflections, with groups of two reflections for monoclinic and groups of four reflections for triclinic symmetries. Accordingly, this feature was used to determine the correct lattice symmetry (Fig. S1 in Ref. [50]), while in other cases the deviation of the monoclinic angle from 90° was so large, that the monoclinic character unequivocally followed from the refined lattice parameters.

The AFM phase (phase II in Table I) was previously shown to be monoclinic with a structural modulation induced by the AFM order, which was represented by only two, weak satellite reflections at positions given by $\mathbf{q}_X = (0, \sigma_b, 0)$ in the x-ray diffraction below $T_{N,1\,\text{bar}} = 81$ K [13]. Presently, we failed to observe any of these satellite reflections, possibly due to the higher background in the present diffraction as it has resulted from contributions from the pressure transmitting medium and DAC components. We did find the monoclinic lattice distortion, e.g., at $T = 6$ K and $p = 0.3$ GPa (the lowest pressure in our measurement) and at $T = 100$ K and $8.9(7) < p < 13.9(1)$ GPa. Observing a continuous dependence on temperature and pressure, we interpret these observations as part of the (p, T) phase diagram where phase II is stable (Table I).

At $T = 293$ K, satellite reflections correspond to a structural modulation related to a densification within the van der

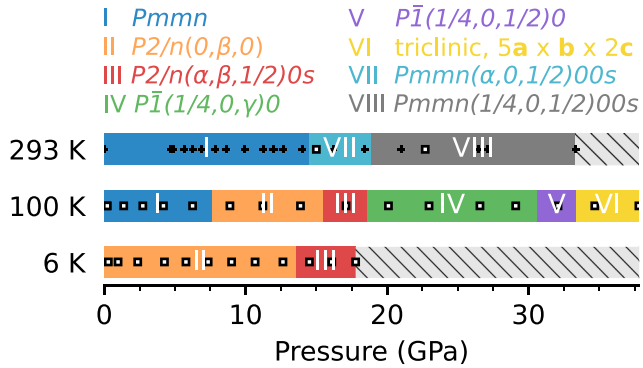

FIG. 2. Schematic representation of the (p, T) phase diagram of FeOCl for temperatures below room temperature and pressures up to 37.8 GPa (compare to Table I). The space group (phase I) and the superspace groups (phases II–VIII) are given at the top of the phase diagram. Data compiled from x-ray diffraction at $T = 6$ and 100 K (this study) and at $T = 293$ K [42]. Each measured (p, T) combination is indicated by a square marker for SXRD or by a cross for x-ray powder diffraction. No data are available for the hatched pressure ranges. The bar diagrams for $T = 6$ and 100 K are used in Figs. 3, and 4 6, and 7.

Waals gap (phases VII and VIII) [42]. Presently, we have found this type of satellite reflections at (p, T) combinations reflecting phases III–VI with monoclinic or triclinic symmetries as opposed to orthorhombic symmetries at $T = 293$ K. Commensurate and incommensurate modulations were distinguished on the basis of structure refinements. Performing the refinement under the assumption of a commensurate modulation leads to different values of the calculated structure factors than the assumption of an incommensurate modulation does. The model with the lowest R value then was taken as one representing the most probable character of the modulation. Further details regarding data processing and structure refinements are given in Ref. [50].

III. DISCUSSION

A. High-pressure–low-temperature phase diagram

At ambient conditions, FeOCl is a paramagnet with orthorhombic symmetry *Pmmn* (phase I) [1]. Upon cooling, an AFM ordered state forms below $T_{N,1\,\mathrm{bar}} = 81$ K (phase II), which is characterized by a modulation wave of magnetic moments with propagation vector $\mathbf{q}_M = (1/2, 0.275, 1/2)$ at 4.2 K, a structural modulation with $\mathbf{q}_X = 2\mathbf{q}_M - \mathbf{a}^* - \mathbf{c}^*$ and a monoclinic lattice distortion [13,48]. Presently, we have found that phase II persists up to at least $p = 14.5$ GPa at $T = 6$ K, and that it is stable between 8.9 and 13.9 GPa at 100 K (Table I and Fig. 2). The paramagnetic phase I exists up to 6.3(3) GPa at 100 K, as identified by the orthorhombic crystal lattice. Given the uncertainty in the transition pressure with $6.3(3) < p_c < 8.9(7)$ GPa at 100 K, we have derived a lower bound for the pressure dependence of the Néel temperature as $\Delta T_N/\Delta p = 2.13$ K/GPa. Linear extrapolation towards $T = 293$ K results in a projected transition pressure of $p_c = 99.5$ GPa. This value is well beyond the measured pressure ranges, and thus explains the absence of an AFM transition at room temperature. Of course, other kinds of phase transitions may take place at pressures beyond 37 GPa, including a high-spin–to–low-spin transition, which typically take place for pressures around 50 GPa [51,52], and an insulator–to–metal transition [53]. We note that the present experiment does not show a reduction of Fe–Ligand bond lengths, as it would be typical for high-spin–to–low-spin transitions [51].

High-pressure diffraction experiments at 293 K have revealed a structural phase transition, with critical pressure $14.0 < p_c < 15.0$ GPa, towards an incommensurately modulated structure (phase VII), which is followed by a lock-in transition towards $\mathbf{q}_X = (1/4, 0, 1/2)$ (phase VIII) [42,43]. Both phases VII and VIII retain the orthorhombic lattice. We have presently observed the structural phase transition upon compression at 100 and 6 K. However, these transitions start from phase II, which is monoclinically distorted due to the AFM order [13]. The monoclinic distortion persists in phase III. Actually, it becomes much stronger at high pressures than the previously extrapolated value of $\gamma = 90.1^\circ$ at 0 K and at ambient pressure. Especially at 6 K, the largest observed monoclinic distortion is $\gamma = 90.64(1)^\circ$ at $p = 17.8$ GPa [Fig. 3(c)]. The present data at 6 K stop with phase III at 17.8 GPa, because of limited amount of beamtime at the synchrotron facility. It is expected that the monoclinic distortion will be larger at even higher pressures. The experimental results do not reveal whether or not phase III involves AFM order (but see discussion below). Despite the reinforcement of the monoclinic distortion, satellite reflections corresponding to the magnetoelastic coupling of a possible AFM order could not be detected. This is caused by their small expected intensities and the high background scattering in the HPLT experiment (see Sec. II D).

The second feature of the structural phase transition is the development of a modulated structure as characterized by a modulation wave vector $\mathbf{q}_X$ (Fig. 4).

This modulation is incommensurate in phase III, where the monoclinic symmetry requires $\sigma_3 = 1/2$, as it is observed indeed [Fig. 4(c)]. The incommensurability of the modulation is further supported by the continuous pressure dependence of the component σ_1 of the modulation wave vector. Unlike orthorhombic symmetry, the monoclinic symmetry does not put restrictions on the σ_2 component. However, the observed small values of σ_2 might not represent a significant deviation from zero [Fig. 4(b)].

Upon further compression at $T = 100$ K, a phase transition occurs at $17.1(2) < p_c < 20.1(2)$ GPa towards phase IV with triclinic symmetry and a similar, incommensurate modulation as in phase III. This symmetry lowering at 100 K takes place instead of the lock-in transition from phase VII to phase VIII at 293 K [54]. A lock-in transition at 100 K proceeds within the triclinic phase at $29.1(3) < p_c < 32.1(3)$ GPa. The resulting phase V transforms into phase VI at $32.1(3) < p_c < 34.7(2)$ GPa. The latter transition is marked by a jump of the the first component of $\mathbf{q}_X$ from 1/4 to 1/5 (Table I). Simultaneously, the quality of the crystal deteriorated, probably because of the large rearrangements of atoms at the V → VI transition, such that a reliable structural solution was not possible at these pressures.

The superstructures of phases V and VI (at 100 K) and phase VIII (at 293 K) are of similar complexity as the superstructure of TiOCl at high pressures [54]. Complex

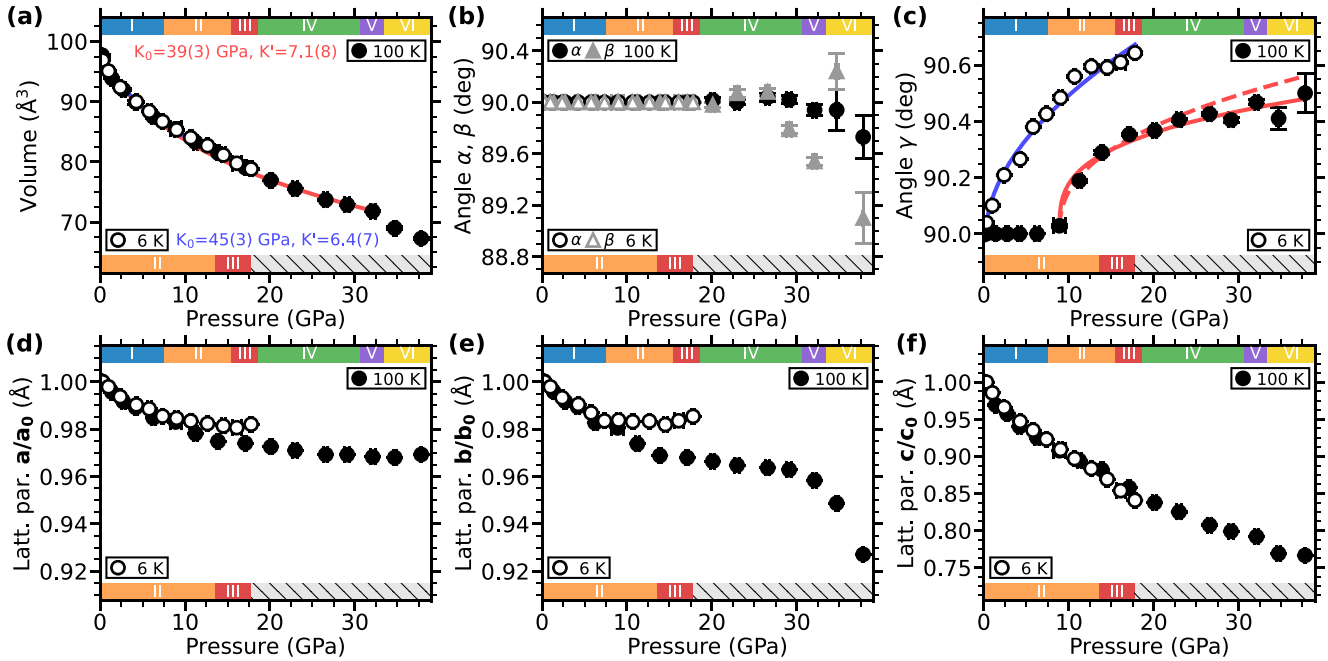

FIG. 3. Lattice parameters as a function of pressure for $T = 6$ K (open symbols) and $T = 100$ K (filled symbols). (a) Volume of the unit cell; lines represent fits to the data points of 3BM-EOS functions [Eq. (1)]. (b) Lattice parameters α and β. (c) γ; solid lines represent fits of Eq. (2) to all data points; the dashed line is a fit to the first five data points above the transition at 100 K (compare Table III). (d) Normalized lattice parameters a/a_0 with $a_{0,6\,\mathrm{K}} = 3.7650(4)$ and $a_{0,100\,\mathrm{K}} = 3.7645(1)$ Å. (e) b/b_0 with $b_{0,6\,\mathrm{K}} = 3.2959(2)$ and $b_{0,100\,\mathrm{K}} = 3.2940(2)$ Å. (f) c/c_0, with $c_{0,6\,\mathrm{K}} = 7.809(9)$ and $c_{0,100\,\mathrm{K}} = 7.882(9)$ Å. Error bars are not shown if they are smaller than the size of the symbol. The upper bar indicates the phase diagram at $T = 100$ K; the lower bar is the phase diagram at $T = 6$ K (compare to Fig. 2).

superstructures at high pressures have been established in other systems too [55–57]. It is the general expectation that compounds attain simple packings at the highest pressures [56]. Obviously, the required high pressures have not been reached in the present experiment.

It is noticed that the structural transitions occur at similar transition pressures at the three available temperatures, with $14.0 < p_c < 15.0$ GPa for I → VII at 293 K, $13.9(1) < p_c < 17.1(2)$ GPa for II → III at 100 K and $12.6(1) < p_c < 14.5(2)$ GPa for II → III at 6 K (Table I). Actually, a decrease with decreasing temperature might be expected for the transition pressure, because of the shrinkage of the lattice upon cooling, and the accompanying closer contacts between the constituent atoms. Such a behavior would also be in agreement with the available uncertainty in p_c.

B. Compressibility and the equation of state

The equation of state (EOS) describes the relation between pressure, volume and temperature of a material. The present data give the volume as a function of pressure at 100 K and 6 K [Fig. 3(a)]. Accordingly, two constant-temperature EOS are obtained as third-order Birch-Murnaghan equations of state (3BM-EOS) [58,59],

$$p = 3K_0 f_E (1 + 2f_E)^{\frac{5}{2}} \left[1 + \tfrac{3}{2}(K' - 4) f_E\right], \qquad (1)$$

where $f_E = \frac{1}{2}[(V_0/V)^{\frac{2}{3}} - 1]$ is the Eularian finite strain. The zero-pressure volume V_0, the bulk modulus at zero pressure K_0 and its derivative K' have been fitted to the (p, V) data, employing the software EOSFIT7-GUI [60] (see Table II).

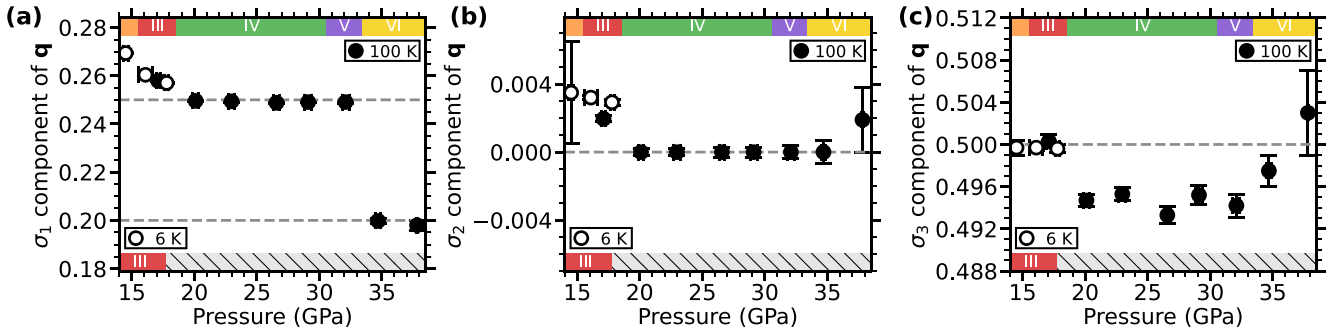

FIG. 4. Components of the modulation wave vector, $\mathbf{q}_X = (\sigma_1, \sigma_2, \sigma_3)$, as a function of pressure for $p > 14$ GPa at $T = 6$ K (open symbols) and $14 < p < 39$ GPa at $T = 100$ K (filled symbols). (a) σ_1 with dashed lines at the rational values 1/5 and 1/4. (b) σ_2 with a dashed line at 0. (c) σ_3 with a dashed line at 1/2. Error bars are not shown if they are smaller than the size of the symbol. The upper bar indicates the phase diagram at $T = 100$ K; the lower bar is the phase diagram at $T = 6$ K (compare to Fig. 2).

TABLE II. Parameters describing the compressibility at constant temperature, as obtained from fitting a third-order Birch-Murnaghan equation of state (EOS) [Eq. (1)] to the experimental data at three different temperatures. Due to the high density of phase transitions, we present at each temperature a single EOS, describing the average behavior of the material over a set of phases (compare Table I). The fits have employed data up to a maximum pressure, as indicated (p_{max}).

T (K)	Phases	p_{max} (GPa)	V_0 (Å^3)	K_0 (GPa)	K'
293[a]	I	14.0	98.3(4)	36(3)	8.2(8)
100	I–IV	32.1	98.0(3)	39(3)	7.1(8)
6	I–II	17.8	97.1(3)	45(3)	6.4(7)

[a]Values at 293 K have been taken from Ref. [42].

The bulk moduli have similar values at the three measured temperatures. The fitted values suggest a slight stiffening of the lattice upon cooling, despite large standard uncertainties. This behavior is in agreement with the expectations based on thermal expansion, which defines smaller volumes and shorter interatomic distances at lower temperatures. FeOCl is less compressible than CrOCl, with $K_{0,293\,K} = 29(2)$ GPa for the latter compound [43]. This is explained by the smaller size of Cr^{3+} than Fe^{3+}, which influences the compression behavior of the layers with M–O and M–Cl bonds.

The compression of FeOCl is highly anisotropic, with, up to phase III, a compression along **c** that is 4–6 times larger than the compressions along **a** and **b** [Figs. 3(d)–3(f)]. The largest compressibility is along the stacking direction of the layers. This kind of anisotropy has been found for FeOCl, CrOCl, VOCl, and TiOCl [42,43,54], as well as for other layered materials [61–63]. It arises from a strong reduction of the interlayer gap across the soft van der Waals interactions.

Previous studies at ambient pressure have revealed a temperature-dependent value of the lattice parameter γ from 90° at T_N towards 90.1° at $T = 0$ K [13]. The monoclinic distortion is the result of magnetoelastic coupling of the AFM order. At room temperature, FeOCl remains orthorhombic ($\gamma = 90°$) up to at least 33 GPa, well beyond the structural transitions. Presently, we have found that pressure strongly enhances the monoclinic distortion, with γ reaching 90.6° at $T = 6$ K for pressures 12–18 GPa [Fig. 3(c)]. Following the earlier analysis of temperature-dependent behavior, we have independently fitted the pressure dependencies of γ at 6 and 100 K, employing the critical relation

$$\gamma - 90° = A\,(p - p_c)^{\beta_c}, \tag{2}$$

where p_c is the critical pressure and β_c is the critical exponent. A fit to all available data points describes their pressure dependence reasonably well. This function could be used to extrapolate γ to pressures higher than measured. A second fit to five data points of lowest pressure more accurately describes critical behavior at 100 K, at the expense of large uncertainties in the fit parameters [Fig. 3(c) and Table III].

Either fit leads to the same critical pressure, $p_c = 8.9(2)$ GPa, for the transition from phase I to phase II. Since FeOCl is already monoclinic at zero pressure for 6 K, such a restricted fit is not meaningful for that temperature.

TABLE III. Parameters obtained by the fit of Eq. (2) to the pressure-dependent values of γ at 100 and 6 K for the full pressure range, and to the first five data points above the critical pressure at 100 K.

T (K)	range	A	p_c (GPa)	β_c
100	full	0.17(2)	8.88(20)	0.30(4)
100	8.9–20.1 GPa	0.14(2)	8.87(20)	0.40(7)
6	full	0.15(2)	0.23(17)	0.53(4)

It is apparent from Fig. 3(c), that the fit with five data points overestimates γ at higher pressures, which is in agreement with a deviation from critical behavior far away from p_c. For 100 K, the two values of the critical exponent agree within their large standard uncertainties. To the extent of these uncertainties, they are in agreement with the 3D Ising, the XY, and the Heisenberg models [13]. Information on the microscopic mechanism of the phase transitions thus cannot be obtained from these data. In any case, the pressure-dependent development of γ suggests that the high-pressure orthorhombic (phase I) to monoclinic (phase II) phase transition at 100 K has a second-order character, which is in agreement with similar transition as a function of temperature at ambient pressure [13].

A second major difference between room-temperature and low-temperature behavior is, that a and b do not exhibit a monotonically decreasing pressure dependence at 6 K (Fig. 3). They even show negative linear compression at some pressures. On the other hand, the angle γ between **a** and **b** strongly deviates from 90° upon increasing pressure. This feature might compensate the apparent negative compressions along **a** and **b**, as it is suggested by the smooth monotonically decreasing pressure dependence of the volume [Fig. 3(a)]. Alternatively phrased: the apparent negative linear compressions along **a** and **b** does not represent a true negative compression, because increasing values of a and b go along with a change of direction of **a** and **b**. Notice that this problem does not exist for lattices with orthorhombic or higher symmetries, where **a**, **b**, and **c** always define the same directions.

C. Pressure dependence of the Néel temperature

The crystal structures of FeOCl comprise a stacking of four-atom thick layers, with the lattice direction **a** and **b** parallel to the layers. Each layer consists of three-atom wide ribbons along **b**, where both Cl and O bridge two consecutive Fe atoms of the central chain of the ribbon. The ribbons are stacked along **a**, such that Cl forms both outer atomic planes of the layers and, along **a**, nearly linear ···Fe–O–Fe–O··· chains are present (Fig. 1). Relevant magnetic exchange interactions are within the layers. The magnetic exchange parameter J_3 is between Fe atoms separated by **a** and follows from one Fe–O–Fe superexchange path (Fig. 5). Each Fe atom has two such contacts, towards ±**a**, respectively. They are equal in the basic structure, but their modulations have a phase difference in the modulated structures. The exchange parameter J_2 is due to direct exchange along the ribbons, and it is strongly AFM. Again, each Fe atom has two equal contacts towards ±**b**, respectively. Their distances are b, and

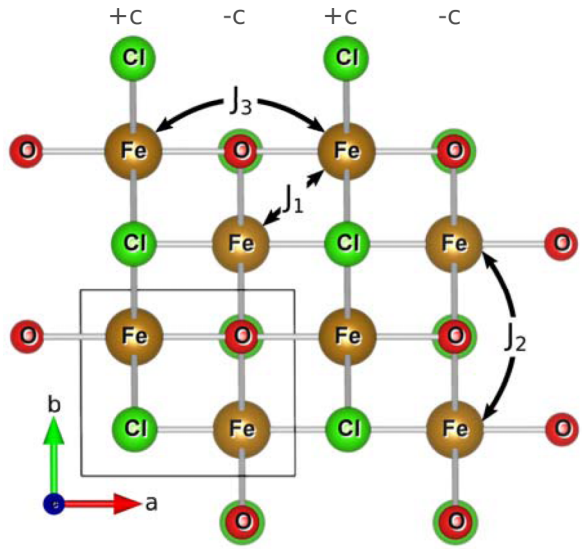

FIG. 5. Projection of one layer FeOCl onto the (**a**, **b**) plane. The unit cell is outlined in the lower left quadrant. Fe atom chains parallel **b** are located above ($+c$) and below ($-c$) the plane of projection. Exchange parameters are defined according to Zhang *et al.* [64]. J_1 is between Fe atoms of neighboring ribbons ("diagonal," **a** and **b** directions). J_2 is between Fe atoms separated by **b**. And J_3 is between Fe atoms separated by **a**.

these are not affected by the modulations, because $\sigma_2 = 0$ in all phases (Table I). Thirdly, each Fe atom is surrounded by four Fe atoms of neighboring ribbons, which are at equal distances and interact via equal exchange parameters J_1 in the orthorhombic phase I. This is the shortest Fe–Fe contact, with d_{diag}[Fe–Fe] = 3.10 Å. Depending on orbital order, contributions to J_1 follow from direct exchange as well as superexchange via two equivalent Fe–O–Fe contacts (designated as "diagonal" contacts in this paper) with bond angles of about 100° [7].

Superexchange interactions are reinforced by shorter Fe–O bond lengths, and bond angles Fe–O–Fe closer to 180° [65]. At 100 K, interatomic distances Fe–O and Fe–Fe along **a** strongly decrease with pressure and the bond angle Fe–O–Fe gradually increases from 149.1(8)° towards 169.0(2)° in phase II [Figs. 6(a) and 6(d)]. This implies that J_3—the largest exchange parameter at ambient conditions [64]—will continuously increase in phases I and II with a concomitantly increase in magnetic stabilization energy in phase II. The J_2 direct exchange parameter increases with increasing pressure due to shortening of the Fe–Fe distance along the ribbons that is equal to the lattice parameter b [Fig. 3(e)]. The ribbons are parallel to the (**b**, **c**) plane. Possible superexchange pathways are Fe–O–Fe and Fe–Cl–Fe contacts, with bond angles close to 90° within this plane. However, the Fe–O distance increases with pressure, supporting the idea that the major interaction

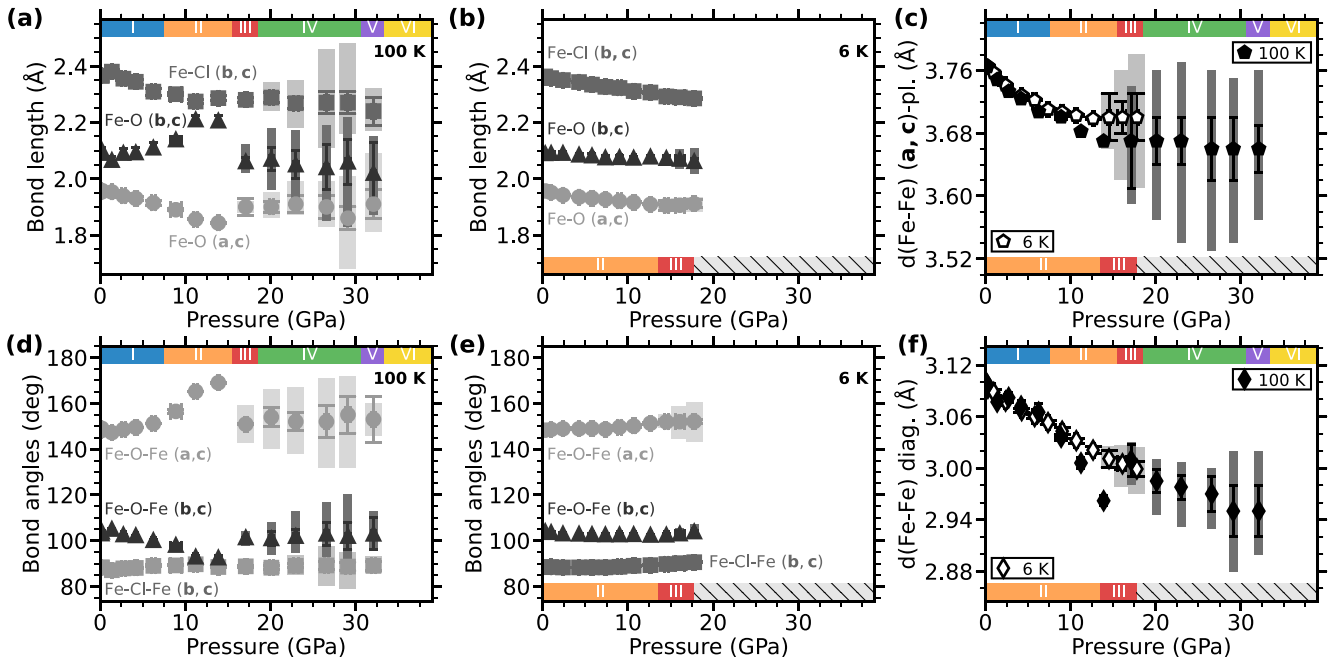

FIG. 6. Pressure dependence of selected interatomic distances and bond angles for the crystal structures at [(a), (c), (d), and (f)] $T = 100$ and [(b), (c), (e), and (f)] 6 K. Vertically placed gray ribbons reflect the range of values as present in the structurally modulated phases, with the superimposed symbol indicating the average value. [(a) and (b)] Distances Fe–O and Fe–Cl within the ribbons FeOCl along **b** parallel to the **b**, **c** plane, and distance Fe–O into the **a** direction. (c) Distance Fe–Fe along **a**; this distance is equal to a in the basic structure. [(d) and (e)] Bond angle Fe–O–Fe and Fe–Cl–Fe within the ribbons FeOCl along **b** parallel to the **b**, **c** plane, and bond angle Fe–O–Fe with the Fe atoms separated by the **a** lattice translation in the basic structure. (f) Distance Fe–Fe between neighboring FeOCl ribbons (diagonal **a**, **b** direction). The shortest distance is shown of two nearly equal Fe–Fe distances (monoclinic symmetry) or of four Fe–Fe distances (triclinic symmetry). Differences between these distances are smaller than 0.021 Å (see Fig. S5 in Ref. [50]). Error bars are not shown if they are smaller than the size of the symbol. The upper bar indicates the phase diagram at $T = 100$ K; the lower bar is the phase diagram at $T = 6$ K (compare to Fig. 2).

along the ribbons is direct exchange between neighboring Fe ions. The most crucial exchange interaction is J_1, since these interactions are responsible for the frustration of AFM order on the orthorhombic lattice [7,11]. The monoclinic lattice distortion ($\gamma \neq 90^\circ$) then stabilizes the observed AFM ground state at the expense of other AFM patterns that are of equal energy on the orthorhombic lattice. The lattice distortion leads to a bifurcation of the shortest Fe–Fe distance of differences of up to Δd_{diag}[Fe–Fe] = 0.021 Å in phase II (Fig. S5 in Ref. [50]).

The strong pressure dependence of the J_3 exchange interaction might be responsible for the pressure dependence of the Néel temperature (Sec. III A). Pressure coefficients $\Delta T_N/\Delta p$ of comparable magnitude have been reported for $FeCO_3$ (1.8 K/GPa) and Co_3O_4 (2.1 K/GPa) [38,39]. For those compounds, however, it was found that the pressure dependence of the exchange was the result of a reduction with pressure of interatomic distances, while variations of bond angles played a minor role [38,39].

The pressure dependence of the structural parameters is much smaller at 6 K than at 100 K (Fig. 6). Accordingly, a smaller pressure dependence can be expected for the magnitudes of the exchange parameters. One possible explanation for this different behavior lies in the fact, that at 6 K, FeOCl is in phase II already for zero pressures [13]. Pressure thus is not required for optimization of the exchange interactions at this temperature.

The pressure dependence of the exchange parameters within the layers can explain the increase of magnetic stabilization energy upon increasing pressure. However, the development of AFM order also requires interlayer interactions. We believe that those interactions are mainly provided by the elastic couplings between the atomic modulations and lattice distortions as defined by the magnetoelastic coupling. The strong pressure dependence of especially the interlayer Cl···Cl distances then may be responsible for an increased three-dimensional character of FeOCl at higher pressures.

D. The structural phase transition

At room temperature, structural transitions have been observed for all compounds *M*OCl (*M* = Ti, V, Cr, Fe) at pressures of approximately 15 GPa [54]. The occurrence of these transitions was rationalized by the requirement of an optimal packing of Cl atoms within the van der Waals interlayer gap [43]. The transition proceeds at a pressure where the Cl···Cl distance would drop below 3.0 Å. The present crystal structures confirm the microscopic model for the structural phase transitions to be valid for FeOCl at 100 K as well as at 6 K. The transitions proceed around 15 GPa, where d[Cl···Cl] ≈3.0 Å (Fig. 7) and the periods of the modulations are similar at all (p, T) combinations for which data are available (Table I). A possibly small temperature dependence of p_c cannot be excluded on the basis of the present data (Table I and Fig. 2; compare Sec. III A).

The structural phase transition proceeds from the paramagnetic state (phase I) at room temperature, while it starts in the AFM ordered state (phase II) at 100 and 6 K. This interference between AFM order (requiring a monoclinic lattice distortion) and optimization of packing of Cl atoms (favored

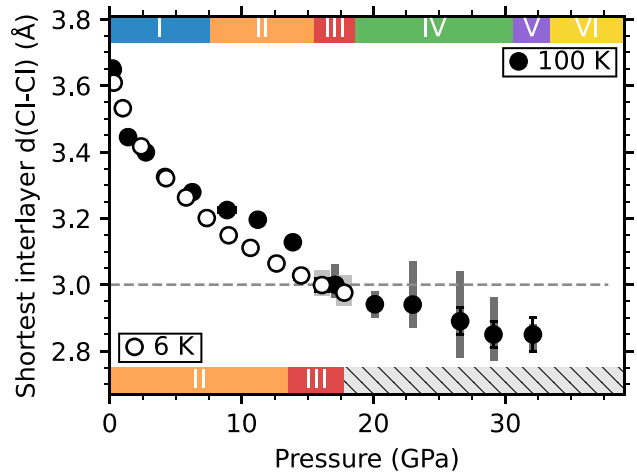

FIG. 7. Shortest interlayer Cl···Cl distance at $T = 6$ K (open symbols) and at $T = 100$ K (filled symbols). Vertically placed gray ribbons reflect the range of values as present in the structurally modulated phases, with the superimposed symbol indicating the average value. The dashed line indicates 3 Å. The shortest distances are shown of two nearly equal Cl···Cl distances (for monoclinic symmetry) or of four Cl···Cl distances (for triclinic symmetry). Differences between these distances go up to 0.02 Å in phase III and up to 0.04 Å in phases IV and V (see Fig. S5 in Ref. [50]). Error bars are not shown if they are smaller than the size of the symbol. The upper bar indicates the phase diagram at $T = 100$ K; the lower bar is the phase diagram at $T = 6$ K (compare to Fig. 2).

by the structural modulation with $\mathbf{q}_X$) is responsible for the peculiar pressure dependence of the crystal structure at 100 K. In phases I and II, bond lengths and bond angles have a strong pressure dependence, as such increasing the strength of the magnetic exchange interactions (Sec. III C). The nonzero value of γ in phase II partially relieves the shortening with pressure of the Cl···Cl distances (Fig. 7). At the transition II → III, the Fe–O distances and Fe–O–Fe angles are restored to their low-pressure values, while the structural modulation becomes responsible for optimizing the packing of Cl atoms in the van der Waals gap (Figs. 6 and 7). The similarity of the structural modulations at the three temperatures also follows from a direct-space plot of the modulated structure. For example, for 100 K, an antiphase buckling of consecutive layers is observed (Fig. 8) that is similar to the antiphase buckling at room temperature (Fig. 1 in Ref. [43]). Furthermore, the similarities of the modulations follow from t plots of the modulation amplitudes and interatomic distances at the three temperatures (Figs. S7– S24 in Ref. [50]).

IV. CONCLUSIONS

FeOCl develops antiferromagnetic (AFM) order upon cooling below $T_{\text{N,1bar}} = 81$ K. Concomitantly, a monoclinic lattice distortion develops [13]. Here, we have reported the crystal structures of FeOCl at 100 K for pressures up to 37.8 GPa, and at 6 K for pressures up to 17.8 K (Table I). Four new phases have been discovered, including structurally modulated phases with monoclinic and triclinic symmetries. A total of eight different phases are thus revealed for FeOCl.

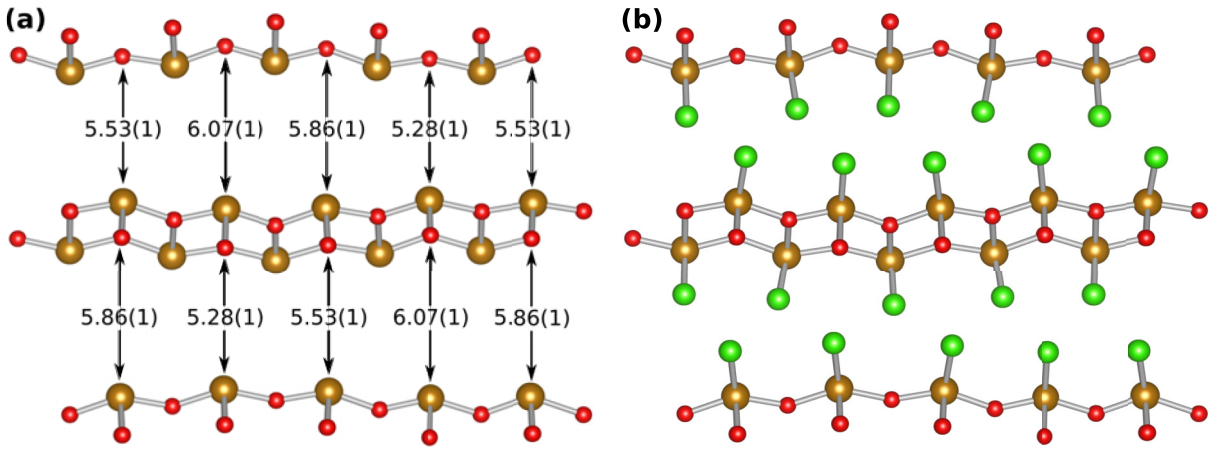

FIG. 8. Projection of the 4**a** × 2**c** approximate superstructure at $T = 100$ K and $p = 23.0(3)$ GPa (phase IV). (a) Cl atoms omitted, showing the Fe-O distances (Å) across the van der Waals gap, and (b) with the Cl atoms shown, revealing their large modulation amplitude along **a**.

We have shown that the Néel temperature increases with increasing pressure. The observed pressure coefficient of $\Delta T_N/\Delta p = 2.13$ K/GPa correlates with the absence of AFM order at room temperature up to, at least, the highest measured pressure of 33.3 GPa. The positive value of the pressure coefficient indicates an enhancement with pressure of the magnetic exchange interactions. Accurate crystal structures have shown, that pressure dependencies of both Fe–O and Fe–Fe bond lengths as well as of Fe–O–Fe bond angles affect the strength of the exchange parameters through modifications of the Fe–Fe direct exchange and the Fe–O–Fe superexchange.

The monoclinic lattice distortion [$\gamma > 90°$; see Fig. 3(c)] is essential for removing the magnetic frustration on the orthorhombic lattice [7,11]. We have found a monoclinic lattice distortion to appear upon entering the AFM phase II on increasing pressure at 100 K, indeed. Furthermore, a strong increase with increasing pressure was observed for this lattice distortion, with values much larger than the largest value that can be achieved at low temperatures for ambient pressure. It is suggested that an enhanced monoclinic lattice distortion might play a role for thin-layer and single-layer FeOCl, CrOCl, and VOCl [26,33].

A structural modulation was previously reported at high pressures for the paramagnetic phase at 293 K with orthorhombic symmetries (phases VII and VIII). Its microscopic origin is an optimization of the packing of Cl atoms within the van der Waals gap [43]. At low temperatures, the structural transition proceeds from the AFM ordered, monoclinic phase II, while the monoclinic distortion continues to increase well into the structurally modulated phases III-V. A small effect was found on the Cl···Cl distances across the van der Waals gap (Fig. 7), thus facilitating a slightly more efficient packing of Cl atoms. Otherwise, the structural modulation is hardly affected by the lattice distortion. The HPLT SXRD experiments do not provide direct information on the magnetic order in the different phases. Nevertheless, the thermal development of interatomic distances suggests that AFM order persists into phase III. Furthermore, other kinds of phase transitions may take place at pressures beyond 37 GPa, including a high-spin–to–low-spin transition [51,52,66], and an insulator–to–metal transition [53].

ACKNOWLEDGMENTS

Single crystals were synthesized by Kerstin Küspert at the Laboratory of Crystallography in Bayreuth. We acknowledge DESY (Hamburg, Germany), a member of the Helmholtz Association HGF, for the provision of experimental facilities. Parts of this research were carried out at PETRA III, using beamline P02.2. Beamtime was allocated for Proposal No. I-20180741. This research has been funded by the Deutsche Forschungsgemeinschaft (DFG; German Research Foundation)–386411512.

[1] M. D. Lind, Refinement of the crystal structure of iron oxychloride, Acta Crystallogr., Sect. B: Struct. Crystallogr. Cryst. Chem. **26**, 1058 (1970).

[2] K. Momma and F. Izumi, VESTA 3 for three-dimensional visualization of crystal, volumetric and morphology data, J. Appl. Crystallogr. **44**, 1272 (2011).

[3] A. Seidel, C. A. Marianetti, F. C. Chou, G. Ceder, and P. A. Lee, S=1/2 chains and spin-Peierls transition in TiOCl, Phys. Rev. B **67**, 020405(R) (2003).

[4] T. Saha-Dasgupta, R. Valentí, H. Rosner, and C. Gros, TiOCl, an orbital-ordered system?, Europhys. Lett. **67**, 63 (2004).

[5] M. Hoinkis, M. Sing, J. Schäfer, M. Klemm, S. Horn, H. Benthien, E. Jeckelmann, T. Saha-Dasgupta, L. Pisani, R. Valentí, and R. Claessen, Electronic structure of the spin-1/2 quantum magnet TiOCl, Phys. Rev. B **72**, 125127 (2005).

[6] M. Hoinkis, M. Sing, S. Glawion, L. Pisani, R. Valentí, S. van Smaalen, M. Klemm, S. Horn, and R. Claessen, One-dimensional versus two-dimensional correlation effects in the oxyhalides TiOCl and TiOBr, Phys. Rev. B **75**, 245124 (2007).

[7] S. Glawion, M. R. Scholz, Y. Z. Zhang, R. Valentí, T. Saha-Dasgupta, M. Klemm, J. Hemberger, S. Horn, M. Sing, and

R. Claessen, Electronic structure of the two-dimensional Heisenberg antiferromagnet VOCl: A multiorbital Mott insulator, Phys. Rev. B **80**, 155119 (2009).

[8] M. Shaz, S. van Smaalen, L. Palatinus, M. Hoinkis, M. Klemm, S. Horn, and R. Claessen, Spin-Peierls transition in TiOCl, Phys. Rev. B **71**, 100405(R) (2005).

[9] C. R. Rotundu, J. Wen, W. He, Y. Choi, D. Haskel, and Y. S. Lee, Enhancement and destruction of spin-Peierls physics in a one-dimensional quantum magnet under pressure, Phys. Rev. B **97**, 054415 (2018).

[10] A. Schönleber, J. Angelkort, S. van Smaalen, L. Palatinus, A. Senyshyn, and W. Morgenroth, Phase transition, crystal structure, and magnetic order in VOCl, Phys. Rev. B **80**, 064426 (2009).

[11] A. C. Komarek, T. Taetz, M. T. Fernández-Díaz, D. M. Trots, A. Möller, and M. Braden, Strong magnetoelastic coupling in VOCl: Neutron and synchrotron powder x-ray diffraction study, Phys. Rev. B **79**, 104425 (2009).

[12] J. Angelkort, A. Wölfel, A. Schönleber, S. van Smaalen, and R. K. Kremer, Observation of strong magnetoelastic coupling in a first-order phase transition of CrOCl, Phys. Rev. B **80**, 144416 (2009).

[13] J. Zhang, A. Wölfel, L. Li, S. van Smaalen, H. L. Williamson, and R. K. Kremer, Magnetoelastic coupling in the incommensurate antiferromagnetic phase of FeOCl, Phys. Rev. B **86**, 134428 (2012).

[14] X. J. Yang, X. M. Xu, J. Xu, and Y. F. Han, Iron oxychloride (FeOCl): An efficient Fenton-like catalyst for producing hydroxyl radicals in°radation of organic contaminants, J. Am. Chem. Soc. **135**, 16058 (2013).

[15] M. Sun, I. Zucker, D. M. Davenport, X. Zhou, J. Qu, and M. Elimelech, Reactive, self-cleaning ultrafiltration membrane functionalized with iron oxychloride nanocatalysts, Environ. Sci. Technol. **52**, 8674 (2018).

[16] M. Sun, C. Chu, F. Geng, X. Lu, J. Qu, J. Crittenden, M. Elimelech, and J. H. Kim, Reinventing Fenton chemistry: Iron oxychloride nanosheet for pH-insensitive H_2O_2 activation, Environ. Sci. Technol. Lett. **5**, 186 (2018).

[17] J. Zhang, G. Liu, and S. Liu, 2D/2D FeOCl/graphite oxide heterojunction with enhanced catalytic performance as photo-Fenton catalyst, New J. Chem. **42**, 6896 (2018).

[18] M. Wang, J. Zhang, Z. Wang, C. Wang, S. van Smaalen, H. Xiao, X. Chen, C. Du, X. Xu, and X. Tao, Broadband CrOCl saturable absorber with a spectral region extension to 10.6 μm, Adv. Opt. Mater. **8**, 1901446 (2020).

[19] X. Zhao, Z. Zhao-Karger, D. Wang, and M. Fichtner, Metal oxychlorides as cathode materials for chloride ion batteries, Angew. Chem. Int. Ed. **52**, 13621 (2013).

[20] P. Gao, C. Wall, L. Zhang, M. A. Reddy, and M. Fichtner, Vanadium oxychloride as electrode material for sodium ion batteries, Electrochem. Commun. **60**, 180 (2015).

[21] X. Zhao, Q. Li, T. Yu, M. Yang, K. Fink, and X. Shen, Carbon incorporation effects and reaction mechanism of FeOCl cathode materials for chloride ion batteries, Sci. Rep. **6**, 19448 (2016).

[22] T. Yu, X. Zhao, L. Ma, and X. Shen, Intercalation and electrochemical behaviors of layered FeOCl cathode material in chloride ion battery, Mater. Res. Bull. **96**, 485 (2017).

[23] T. Yu, Q. Li, X. Zhao, H. Xia, L. Ma, J. Wang, Y. S. Meng, and X. Shen, Nanoconfined iron oxychloride material as a high-performance cathode for rechargeable chloride ion batteries, ACS Energy Lett. **2**, 2341 (2017).

[24] N. Mounet, M. Gibertini, P. Schwaller, D. Campi, A. Merkys, A. Marrazzo, T. Sohier, I. E. Castelli, A. Cepellotti, G. Pizzi, and N. Marzari, Two-dimensional materials from high-throughput computational exfoliation of experimentally known compounds, Nat. Nanotechnol. **13**, 246 (2018).

[25] N. Miao, B. Xu, L. Zhu, J. Zhou, and Z. Sun, 2D intrinsic ferromagnets from van der Waals antiferromagnets, J. Am. Chem. Soc. **140**, 2417 (2018).

[26] A. K. Nair, S. Rani, M. V. Kamalakar, and S. J. Ray, Bi-stimuli assisted engineering and control of magnetic phase in monolayer CrOCl, Phys. Chem. Chem. Phys. **22**, 12806 (2020).

[27] X. Qing, H. Li, C. Zhong, P. Zhou, Z. Dong, and J. Liu, Magnetism and spin exchange coupling in strained monolayer CrOCl, Phys. Chem. Chem. Phys. **22**, 17255 (2020).

[28] D. Torelli, H. Moustafa, K. W. Jacobsen, and T. Olsen, High-throughput computational screening for two-dimensional magnetic materials based on experimental databases of three-dimensional compounds, npj Comput. Mater. **6**, 158 (2020).

[29] W. Wang, R. Sun, S. He, Z. Jia, C. Su, Y. Li, and Z. Wang, Atomic structure, work function and magnetism in layered single crystal VOCl, 2D Mater. **8**, 015027 (2021).

[30] S. Wang, J. Wang, and M. Khazaei, Discovery of stable and intrinsic antiferromagnetic iron oxyhalides monolayers, Phys. Chem. Chem. Phys. **22**, 11731 (2020).

[31] S. Yang, T. Zhang, and C. Jiang, Van der Waals magnets: Material family, detection and modulation of magnetism, and perspective in spintronics, Adv. Sci. **8**, 2002488 (2021).

[32] J. Zhang, X.-L. Jiao, Y.-G. Xia, F.-F. Liu, Y.-P. Pang, X.-F. Zhao, and D.-R. Chen, Enhanced catalytic activity in liquid-exfoliated FeOCl nanosheets as a fenton-like catalyst, Chem. Eur. J. **22**, 9321 (2016).

[33] A. M. Ferrenti, S. Klemenz, S. Lei, X. Song, P. Ganter, B. V. Lotsch, and L. M. Schoop, Change in magnetic properties upon chemical exfoliation of FeOCl, Inorg. Chem. **59**, 1176 (2020).

[34] K. Awaga, T. Sekine, M. Okawa, W. Fujita, S. M. Holmes, and G. S. Girolami, High-pressure effects on a manganese hexacyanomanganate ferrimagnet with $T_N = 29$ K, Chem. Phys. Lett. **293**, 352 (1998).

[35] W.-B. Zhang, Y.-L. Hu, K.-L. Han, and B.-Y. Tang, Pressure dependence of exchange interactions in NiO, Phys. Rev. B **74**, 054421 (2006).

[36] A. G. Gavriliuk, I. S. Lyubutin, S. S. Starchikov, A. A. Mironovich, S. G. Ovchinnikov, I. A. Trojan, Y. Xiao, P. Chow, S. V. Sinogeikin, and V. V. Struzhkin, The magnetic P-T phase diagram of langasite $Ba_3TaFe_3Si_2O_{14}$ at high hydrostatic pressures up to 38 GPa, Appl. Phys. Lett. **103**, 162402 (2013).

[37] I. S. Lyubutin, S. S. Starchikov, A. G. Gavriliuk, I. A. Troyan, Y. A. Nikiforova, A. G. Ivanova, A. I. Chumakov, and R. Rüffer, Magnetic phase separation and strong enhancement of the Néel temperature at high pressures in a new multiferroic $Ba_3TaFe_3Si_2O_{14}$, JETP Lett. **105**, 26 (2017).

[38] N. O. Golosova, D. P. Kozlenko, L. S. Dubrovinsky, V. Cerantola, M. Bykov, E. Bykova, S. E. Kichanov, E. V. Lukin, B. N. Savenko, A. V. Ponomareva, and I. A. Abrikosov, Magnetic and structural properties of $FeCO_3$ at high pressures, Phys. Rev. B **96**, 134405 (2017).

[39] N. O. Golosova, D. P. Kozlenko, D. Nicheva, T. Petkova, S. E. Kichanov, E. V. Lukin, G. Avdeev, P. Petkov, and B. N. Savenko, High pressure effects on the crystal and magnetic structures of Co_3O_4, J. Magn. Magn. Mater. **508**, 166874 (2020).

[40] N. O. Golosova, D. P. Kozlenko, S. E. Kichanov, E. V. Lukin, A. V. Rutkauskas, K. V. Glazyrin, and B. N. Savenko, Magnetic and structural properties of Fe-doped layered cobaltite $TbBaCo_{1.91}Fe_{0.09}O_{5.5}$ at high pressures, J. Magn. Magn. Mater. **494**, 165801 (2020).

[41] D. Bloch, The 10/3 law for the volume dependence of superexchange, J. Phys. Chem. Solids **27**, 881 (1966).

[42] M. Bykov, E. Bykova, S. van Smaalen, L. Dubrovinsky, C. McCammon, V. Prakapenka, and H.-P. Liermann, High-pressure behavior of FeOCl, Phys. Rev. B **88**, 014110 (2013).

[43] M. Bykov, E. Bykova, L. Dubrovinsky, M. Hanfland, H.-P. Liermann, and S. van Smaalen, Pressure-induced normal-incommensurate and incommensurate-commensurate phase transitions in CrOCl, Sci. Rep. **5**, 9647 (2015).

[44] H.-P. Liermann, Z. Konôpková, W. Morgenroth, K. Glazyrin, J. Bednarčik, E. E. McBride, S. Petitgirard, J. T. Delitz, M. Wendt, Y. Bican, A. Ehnes, I. Schwark, A. Rothkirch, M. Tischer, J. Heuer, H. Schulte-Schrepping, T. Kracht, and H. Franz, The extreme conditions beamline P02.2 and the extreme conditions science infrastructure at PETRA III, J. Synchrotron Radiat. **22**, 908 (2015).

[45] A. Dewaele, M. Torrent, P. Loubeyre, and M. Mezouar, Compression curves of transition metals in the Mbar range: Experiments and projector augmented-wave calculations, Phys. Rev. B **78**, 104102 (2008).

[46] Rigaku Oxford Diffraction, *CrysAlis*^{Pro} software system, Rigaku Corporation (2019), https://www.rigaku.com/de/products/smc/crysalis.

[47] V. Petříček, M. Dušek, and L. Palatinus, Crystallographic computing system JANA2006: General features, Z. Kristallogr. - Cryst. Mater. **229**, 345 (2014).

[48] A. Adam and G. Buisson, Structure magnétique cycloïdale de FeOCl, Phys. Status Solidi A **30**, 323 (1975).

[49] H. T. Stokes, B. J. Campbell, and S. van Smaalen, Generation of (3 + d)-dimensional superspace groups for describing the symmetry of modulated crystalline structures, Acta Crystallogr. A Found Crystallogr **67**, 45 (2011).

[50] See Supplemental Material at http://link.aps.org/supplemental/10.1103/PhysRevB.105.184109 for details about data processing and structure refinements, as well as for values of experimental and structural parameters and t-plots of interatomic distances, which includes Refs. [67–72].

[51] M. Merlini, M. Hanfland, M. Gemmi, S. Huotari, L. Simonelli, and P. Strobel, Fe^{3+} spin transition in $GaFe_2O_4$ at high pressure, Am. Mineral. **95**, 200 (2010).

[52] I. S. Lyubutin and A. G. Gavriliuk, Research on phase transformations in 3d-metal oxides at high and ultrahigh pressure: State of the art, Phys. Usp. **52**, 989 (2009).

[53] C. A. Kuntscher, S. Frank, A. Pashkin, M. Hoinkis, M. Klemm, M. Sing, S. Horn, and R. Claessen, Possible pressure-induced insulator-to-metal transition in low-dimensional TiOCl, Phys. Rev. B **74**, 184402 (2006).

[54] M. Bykov, Structural aspects of pressure- and temperature-induced phase transitions in low-dimensional systems, Ph.D. thesis, University of Bayreuth, 2015, https://epub.uni-bayreuth.de/2085.

[55] C. Hejny and V. S. Minkov, High-pressure crystallography of periodic and aperiodic crystals, IUCrJ **2**, 218 (2015).

[56] C. V. Storm, J. D. McHardy, S. E. Finnegan, E. J. Pace, M. G. Stevenson, M. J. Duff, S. G. MacLeod, and M. I. McMahon, Behavior of rubidium at over eightfold static compression, Phys. Rev. B **103**, 224103 (2021).

[57] E. Boldyreva, Glycine: The gift that keeps on giving, Isr. J. Chem. **61**, 828 (2021).

[58] F. Birch, Finite elastic strain of cubic crystals, Phys. Rev. **71**, 809 (1947).

[59] R. J. Angel, Equations of state, Rev. Mineral. Geochem. **41**, 35 (2000).

[60] J. Gonzalez-Platas, M. Alvaro, F. Nestola, and R. Angel, EosFit7-GUI: A new graphical user interface for equation of state calculations, analyses and teaching, J. Appl. Crystallogr. **49**, 1377 (2016).

[61] R. W. Lynch and H. G. Drickamer, Effect of high pressure on the lattice parameters of diamond, graphite, and hexagonal boron nitride, J. Chem. Phys. **44**, 181 (1966).

[62] K. Knorr, L. Ehm, M. Hytha, B. Winkler, and W. Depmeier, The high pressure behaviour of SnS_2: X-ray powder diffraction and quantum mechanical calculations up to 10 GPa, Phys. Status Solidi B **223**, 435 (2001).

[63] M. O. Filsø, E. Eikeland, J. Zhang, S. R. Madsen, and B. B. Iversen, Atomic and electronic structure transformations in SnS_2 at high pressures: A joint single crystal X-ray diffraction and DFT study, Dalton Trans. **45**, 3798 (2016).

[64] F. Zhang, Y.-C. Kong, R. Pang, L. Hu, P.-L. Gong, X.-Q. Shi, and Z.-K. Tang, Super-exchange theory for polyvalent anion magnets, New J. Phys. **21**, 053033 (2019).

[65] D. I. Khomskii, *Transition Metal Compounds* (Cambridge University Press, Cambridge, UK, 2014).

[66] J.-F. Lin, S. Speziale, Z. Mao, and H. Marquardt, Effects of the electronic spin transitions of iron in lower mantle minerals: Implications for deep mantle geophysics and geochemistry, Rev. Geophys. **51**, 244 (2013).

[67] P. J. Becker and P. Coppens, Extinction within the limit of validity of the Darwin transfer equations. I. General formalism for primary and secondary extinction and their applications to spherical crystals, Acta Cryst. A **30**, 129 (1974).

[68] E. Bykova, Single-crystal x-ray diffraction at extreme conditions in mineral physics and material sciences, Ph.D. thesis, University of Bayreuth, Bayreuth, 2015, https://epub.uni-bayreuth.de/2124/.

[69] K. Friese, A. Grzechnik, J. M. Posse, and V. Petříček, Refinement of high pressure single-crystal diffraction data using Jana2006, High Press. Res. **33**, 196 (2013).

[70] S. Klotz, J.-C. Chervin, P. Munsch, and G. Le Marchand, Hydrostatic limits of 11 pressure transmitting media, J. Phys. D: Appl. Phys. **42**, 075413 (2009).

[71] S. van Smaalen, *Incommensurate Crystallography*, IUCr Monography on Crystallography No. 21 (Oxford University Press, Oxford, 2012).

[72] T. Wagner and A. Schönleber, A non-mathematical introduction to the superspace description of modulated structures, Acta Crystallogr. B Struct. Sci. **65**, 249 (2009).